Journal of Materials Chemistry C

ROYAL SOCIETY OF CHEMISTRY

PAPER

View Article Online
View Journal

Cite this: DOI: 10.1039/d6tc00041j

Two-dimensional hexagonal boron nitride-ferrofluid hybrids enable efficient magnetic cooling

Nishant Tiwari,[ab] Alexey Kartsev,[cde] Saswata Goswami,[f] Alexander Arkadyevich Safronov,[e] Chandra Sekhar Tiwary*[af] and Varun Chaudhary *[b]

Received 6th January 2026,
Accepted 9th April 2026

DOI: 10.1039/d6tc00041j

rsc.li/materials-c

Overheating remains a critical limitation in high-performance electronic and computing systems, necessitating the development of efficient thermal management fluids. In this work, a magnetically responsive hybrid ferrofluid was developed by incorporating two-dimensional hexagonal boron nitride (2D-hBN) nanosheets into a Mn–Zn–ferrite-based ferrofluid. The hybrid system retains magnetic responsiveness while leveraging the high in-plane thermal conductivity and chemical stability of 2D-hBN nanosheets. Structural, spectroscopic, and magnetic characterizations confirm the successful incorporation of 2D-hBN within the ferrofluid without compromising the magnetic functionality of the ferrite nanoparticles. The thermal conductivity of the hybrid fluid increased from 0.294 to 0.582 W m^{-1} K^{-1}, representing nearly a twofold enhancement compared to the base ferrofluid. Cooling experiments performed under different magnetic field strengths demonstrate field-dependent thermal performance. At an applied magnetic field of 0.30 Tesla, the hybrid ferrofluid achieved a maximum temperature drop of ~35 °C, corresponding to more than 50% improvement in cooling efficiency compared to the base ferrofluid under identical heat load conditions. These results highlight the potential of 2D-hBN-modified ferrofluids as promising magnetothermal cooling media for passive and magnetically assisted thermal management applications in next-generation electronic systems.

Introduction

Efficient heat dissipation has become a critical challenge in modern electronics, energy systems, and computing infrastructure, where increasing power densities generate substantial thermal loads.[1,2] Inadequate thermal management not only limits the device performance and reliability, but also contributes significantly to the overall energy consumption, particularly in data processing and high-performance computing facilities. Developing cooling technologies that are both energy-efficient and environmentally sustainable is, therefore, an urgent research priority.[3,4] The development of efficient, compact, and environmentally friendly cooling technologies has intensified research into advanced heat transfer fluids as alternatives to conventional vapor-compression and mechanically pumped systems.[5] Among these, ferrofluids-stable colloidal suspensions of magnetic nanoparticles in a carrier liquid have received considerable attention due to their ability to interact with external magnetic fields. When exposed to a thermal gradient under a magnetic field, ferrofluids undergo thermomagnetic convection, in which spatial variations in magnetization generate body forces that drive fluid motion and enhance heat transport.[6,7] Such magnetically controlled heat transfer enables passive and vibration-free operation, offering advantages in system simplicity and energy efficiency. Recent studies have demonstrated the feasibility of ferrofluid-based loops for long-distance heat transfer and magnetic cooling applications, highlighting their potential for integration in electronic cooling and energy systems.[8–10]

Despite these advantages, the overall cooling performance of ferrofluids is often limited by their relatively low thermal conductivity compared with solid heat-spreading materials. In parallel, extensive research on non-magnetic nanofluids and hybrid nanofluids-containing additives such as graphene, carbon nanotubes, or metallic nanoparticles-has demonstrated significant improvements in thermal transport properties of conventional base fluids.[11–14] Previous studies have examined ferrofluid-based heat-transfer behaviour in various magnetohydrodynamic and

[a] Department of Metallurgical and Materials Engineering, Indian Institute of Technology Kharagpur, West Bengal 721302, India. E-mail: chandra.tiwary@metal.iitkgp.ac.in
[b] Department of Mechanical Engineering, Chalmers University of Technology, Gothenburg SE-41296, Sweden. E-mail: varunc@chalmers.se
[c] Bauman Moscow State Technical University, Moscow, 105005, Russia
[d] Peoples' Friendship University of Russia – RUDN University, Moscow 117198, Russia
[e] MIREA-Russian Technological University, 119454 Moscow, Russia
[f] School of Nano Science and Technology, Indian Institute of Technology Kharagpur, West Bengal 721302, India

geometrically complex thermal systems, including porous domains, grooved channels, and non-uniform heating configurations.[15–18] However, these studies have largely focused on fluid-flow and thermal-system design, whereas the deliberate materials engineering of ferrofluids using two-dimensional thermally conductive additives for magnetothermal cooling remains largely unexplored. Integrating thermally conductive nanomaterials into ferrofluids could therefore provide a promising strategy to simultaneously enhance both thermal transport and magnetic-field-driven fluid motion.

Hexagonal boron nitride (hBN), a two-dimensional layered material structurally analogous to graphite, has recently emerged as a promising thermally conductive yet electrically insulating additive for thermal management applications.[19,20] hBN nanosheets possess high in-plane thermal conductivity (hundreds of W m^{-1} K^{-1}), excellent thermal and chemical stability, and mechanical robustness.[21,22] These properties have led to their widespread use in polymer composites, coatings, and lubricants designed for efficient heat dissipation.[23–25] Incorporating hBN into ferrofluids offers several potential benefits: (i) improved thermal conductivity through the formation of conductive heat pathways, (ii) mitigation of localized hot spots *via* superior heat spreading, (iii) enhanced thermal stability of the suspension under cyclic operation, and (iv) electrical insulation, which is critical in electronic cooling applications. The anisotropic thermal properties of hBN further enable directional heat transfer depending on flake alignment within the fluid. However, achieving these benefits requires stable dispersion and effective interfacial interactions between hBN nanosheets and magnetic nanoparticles, since excessive aggregation or increased viscosity may adversely affect fluid mobility and heat transport.[26–28] These aspects are critical for realizing the full potential of hBN-based ferrofluids in magnetothermal applications.

Motivated by these considerations, the present work investigates the incorporation of two-dimensional hBN nanosheets into a Mn–Zn–ferrite-based ferrofluid to enhance its thermal and magnetic field-responsive properties. The influence of hBN on structural, thermal, and magnetic characteristics is systematically examined through structural and spectroscopic characterization, thermal measurements, and magnetic analyses, complemented by first-principles density functional theory (DFT) calculations. These combined experimental and theoretical approaches provide insights into how interfacial interactions between hBN nanosheets and ferrite nanoparticles influence magnetothermal performance. Emphasis is placed on understanding the relationship between interfacial structure and cooling efficiency under cyclic magnetic-field operation. The results contribute to the design of ferrofluid systems that integrate two-dimensional materials for controlled and energy-efficient heat transport.

Materials and methods

Experimental details

Two-dimensional hexagonal boron nitride (2D-hBN) nanosheets were prepared *via* liquid-phase exfoliation of bulk hBN powder (5 g, 97% purity, Sigma-Aldrich). The powder was dispersed in 50 mL of isopropyl alcohol (IPA, >99% purity) and subjected to probe sonication for 2 h to exfoliate the layered hBN into few-layer nanosheets. The resulting dispersion was centrifuged for 1 h to remove unexfoliated particles, and the supernatant containing exfoliated nanosheets was collected.

After synthesis, 1 wt% of the hBN was added to a commercially available water-based ferrofluid (Ferrotec Inc.), composed of Mn–Zn–ferrite ($Mn_{0.7}Zn_{0.3}Fe_2O_4$) nanoparticles (1–4 vol%, size 3–5 nm), an organomethoxysilane dispersant (7–27 vol%), and deionized water (69–92 vol%). We have confirmed the particle size using HR-TEM (high resolution-transmission electron microscopy), as shown in Fig. S1. To ensure uniform dispersion and long-term stability, the mixture was subjected to bath sonication for 5 h. No additional chemical functionalization of hBN was performed, as the sonication process, together with the surfactant system of the commercial ferrofluid, provided sufficient stabilization.

The concentration of 2D-hBN nanosheets was fixed at 1 wt% based on dispersion stability and magnetic compatibility considerations. Zeta potential measurements performed using a Litesizer instrument showed that the base ferrofluid exhibits a value of −31.32 mV, indicating good colloidal stability, while the addition of hBN reduces the value to −15.86 mV. Since further addition of hBN could reduce electrostatic stabilization and promote particle agglomeration, the concentration was limited to 1 wt%. In addition, excessive incorporation of non-magnetic nanosheets may negatively affect the magnetization and field-induced structuring of the ferrofluid.[29,30] Therefore, 1 wt% was selected as a balanced loading that maintains dispersion stability while enabling measurable enhancement in thermal performance.

Structural, morphological, and spectroscopic characterizations of 2D-hBN and 2D-hBN/ferrofluid were carried out using XRD, SEM, and Raman Spectroscopy techniques. Detailed crystallographic analysis was performed with a Bruker D8 advance diffractometer (Cu-Kα radiation, 2θ range 20–70°), while microstructural features were examined using a ZEISS GEMINI 600 FE-SEM and a JEOL NEOARM 200 kV HR-TEM. Samples for structural, morphological, and magnetic characterization were prepared using a drop-casting technique due to the viscous liquid nature of the composite ferrofluid. For X-ray diffraction (XRD) and scanning electron microscopy (SEM) analyses, a small amount of the sample was drop-cast onto a clean silicon wafer (Si-wafer) substrate and allowed to dry naturally overnight in a closed environment to minimize possible contamination. After complete drying, the samples were used for the respective measurements. For transmission electron microscopy (TEM) analysis, the sample was drop-casted onto a carbon-coated copper grid, and allowed to dry prior to imaging. The thickness and lateral dimensions of the 2D-hBN sheets were characterized using an atomic force microscope (Agilent Technologies, model 5500). Raman spectra were collected at room temperature with a WITec UHTS 300 VIS Raman spectrometer equipped with a 532 nm excitation laser 15 mW laser power irradiation. X-ray photoelectron spectroscopy (XPS) measurements were carried out using a PHI 5000 VersaProbe III system (ULVAC-PHI, Physical

Electronics). Magnetic characterization of the homogenized fluid was conducted using a vibrating sample magnetometer (Lake Shore Cryotronics, USA), including *M–T* measurements under field-cooled warming (FCW) and field-cooling (FC) conditions at 0.1 T/1000 Oe. For magnetic characterization, the sample was similarly drop-cast onto a silicon wafer substrate. Since accurate mass determination is essential for magnetic measurements, the silicon wafer was weighed prior to sample deposition and again after the sample was completely dried overnight. The difference between the two measurements was taken as the mass of the deposited sample. The dried sample was then mounted on the quartz sample holder of the vibrating sample magnetometer (VSM) for magnetic measurements. Thermal conductivity was evaluated using a hot disk thermal constants analyzer (TPS 2500 S).

To ensure the reliability and reproducibility of the experimental results, all measurements were repeated multiple times under identical experimental conditions. Structural and morphological characterizations, including XRD and SEM, were repeated at least twice to confirm phase purity and microstructural consistency. Magnetic measurements were performed using repeated runs of the same sample to verify the stability of the magnetization response. Thermal conductivity measurements were conducted in multiple trials, and the reported values represent the average of repeated measurements. Cooling performance experiments were also repeated, including cyclic magnetic field application tests, to verify the repeatability and stability of the temperature response over extended operation periods. Where applicable, error bars represent the standard deviation obtained from repeated measurements.

Working principle and device set-up

The dimensions of the Cu loop are provided in Fig. S2 of the SI. The loop has an inner diameter of approximately 28 cm and an outer diameter of approximately 30 cm. The volume of ferrofluid used in the Cu loop was approximately 40 ± 2 mL. An Nd–Fe–B cuboid magnet, positioned facing the heat source, generates the magnetic field. The magnetic field strength was measured using a Gauss meter (Hirst GM08) at the position closest to the permanent magnet, corresponding to the section of the loop exposed to the maximum magnetic field. To ensure measurement accuracy, approximately ten readings were recorded at the same position and averaged to obtain the final magnetic field value. For measurements at reduced magnetic field strengths, the distance between the magnet and the loop was systematically increased. Initially, a 1 mm thick insulating glass plate was inserted between the magnet and the loop to reduce the effective magnetic field. Further reductions were achieved by progressively increasing the separation between the magnet and the loop, and the magnetic field strength was measured at each step using the Gauss meter.

The ferrofluid itself is a colloidal suspension of thermomagnetic nanoparticles dispersed in either water or oil, exhibiting liquid-like flow while responding to external magnetic fields. Its magnetization is strongly temperature dependent: the response decreases as the temperature rises, and the nanoparticles become paramagnetic once the Curie temperature is exceeded. When a temperature gradient is established between the heat source and the heat sink, a corresponding gradient in the magnetic susceptibility of the ferrofluid is induced. The interplay between this susceptibility gradient and the applied magnetic field generates a non-uniform magnetic body force, driving thermo-magnetic convection within the fluid. In the closed-loop configuration, the magnetic field gradient is introduced by placing a permanent magnet near the heat source, while the heat sink is positioned opposite to it. Initially, the ferrofluid at ambient temperature is drawn toward the magnet, where it absorbs heat from the heat source. As its temperature increases, its magnetic susceptibility decreases, weakening its attraction to the magnet. This heated fluid is displaced by cooler incoming ferrofluid, which takes its place near the magnet. The warmer fluid continues along the loop, transferring absorbed heat to the sink, where it is cooled, thereby completing the convection cycle.

For device fabrication, a copper tube with an inner diameter of 5 mm was used to accommodate the heat source and heat sink, as shown in Fig. S2. Joule heating at controlled heat flux levels was achieved using a Kanthal wire (1 mm outer diameter, 1.68 Ω m^{-1} resistivity), with 30 cm of the wire wound over a 4 cm section of the heat source. Surface temperatures of the heat load were monitored using K-type thermocouples (TC) (PICOLOG, UK) with an accuracy of ±0.5 °C, which were fixed in place and electrically insulated by wrapping the region with Kapton tape. The magnetic driving force for ferrofluid motion was supplied by a cubic Nd–Fe–B permanent magnet (0.3 T, 25 mm side length). The magnet was strategically positioned at the end of the heat load, where the thermal gradient was the steepest, to establish a suitable field gradient and enhance fluid circulation during magnetic cooling.[31] All the nomenclature/symbols of used in present work are summarized in Table 1.

Result and discussion

Rheology and structural characterization

The rheological measurements were performed to evaluate the effect of 2D-hBN nanosheet incorporation on the flow behaviour of the ferrofluid. Viscosity measurements were carried out at shear rates of 30, 50, and 100 s^{-1} for both the base ferrofluid and the 2D-hBN/ferrofluid hybrid, and the results are presented

Table 1 Nomenclature/symbols used in the present work

Sr. no.	Nomenclature/symbols	Unit
1	Temperature	°C (degree celcius) or K (kelvin)
2	Temperature difference (ΔT)	°C or K
3	Magnetic field strength ($\mu_o H$)	Tesla (T)
4	Magnetization (M)	emu g^{-1}
5	Zeta potential	mV (milli volt)
6	Thermal conductivity (κ)	W m^{-1} K^{-1}
7	Viscosity (μ)	cP
8	Shear stress	s^{-1}
9	Millimetre	mm
10	Centimetre	cm
11	Heat load	W (Watt)
12	Time	Minute (min.) or seconds (s)

in Fig. S3. The results show that the viscosity of both fluids increases approximately linearly with increasing shear rate within the investigated range. The 2D-hBN/ferrofluid hybrid exhibits slightly higher viscosity compared to the base ferrofluid, which can be attributed to the presence of suspended 2D-hBN nanosheets that increase hydrodynamic resistance within the fluid. The moderate increase in viscosity suggests that the nanosheets are well dispersed and do not lead to significant agglomeration or flow obstruction.

To elucidate the structural characteristics of the materials, we first performed X-ray diffraction (XRD) analysis of both bulk hBN and exfoliated 2D-hBN. As shown in Fig. S4(a), the diffraction pattern displays distinct peaks at 2θ = 26.1°, 41.3°, 43.8°, 50.4°, and 55.6°, which correspond to the (002), (100), (101), (102), and (004) crystallographic planes of hexagonal boron nitride,[32] consistent with the standard JCPDS card No. 34-0421. Scanning electron microscopy (SEM) images of the exfoliated product, presented in Fig. S4(b), reveal a characteristic flake-like morphology, confirming the formation of a two-dimensional layered structure. To probe the chemical composition and bonding environment, X-ray photoelectron spectroscopy (XPS) was carried out, where N 1s peak at ~398 eV in Fig. S4(c) and the B 1s peak appears at ~190.5 eV Fig. S4(d).[33,34] The thickness and lateral dimensions of the 2D flakes were further examined by atomic force microscopy (AFM). As illustrated in Fig. S4(e), the exfoliated sheets exhibit a thickness of approximately 5–10 nm, corresponding to a few-layer to multilayer configuration, with lateral sizes ranging from 50 to 200 μm. The AFM images also demonstrate a uniform spatial distribution of the flakes across the substrate surface. The 2D-hBN exhibits a characteristic Raman peak in the range of (1366–1373 cm^{-1}),[35,36] corresponding to the E_{2g} phonon mode. In the present study, the exfoliated 2D hBN flakes showed a Raman peak at 1368.3 cm^{-1}, as illustrated in Fig. S4(g). These well-defined 2D-hBN sheets were subsequently dispersed in the ferrite (Mn–Zn) particle-based ferrofluid to prepare the hybrid system, after which the structural characterizations of both the base ferrofluid and the 2D-hBN/ferrofluid composite were systematically investigated. To get to know the composition of Mn–Zn–ferrite particle ($Mn_{0.7}Zn_{0.3}Fe_2O_4$), we have performed EDS (energy dispersive spectroscopy) using SEM, as shown in Fig. S4(i) and (j). Along with this elemental mapping of Mn–Zn–ferrite particles are also shown in Fig. S5(a)–(f).

Fig. 1(a) shows the X-ray diffraction (XRD) patterns of the base ferrofluid and the 2D-hBN/ferrofluid. The base ferrofluid exhibits (black) sharp reflections at 2θ = 30.1°, 35.9°, 42.4°, 52.8°, 56.5°, and 62.0°, which can be indexed to the (220), (311), (400), (422), (511), and (440) crystallographic planes of a ferrite spinel structure,[37] consistent with JCPDS card No. 10-0467. Upon incorporation of 2D-hBN (red), the composite pattern reveals an additional reflection at ~26.4°, corresponding to the (002) basal plane of hexagonal boron nitride, as shown in Fig. 1(a). The structural coupling between the ferrite nanoparticles and the 2D-hBN nanosheets was further investigated using Raman spectroscopy and high-resolution transmission electron microscopy (HR-TEM). The Raman spectrum of the composite, shown in Fig. 1(b), exhibits prominent modes of both constituents: the ferrite phase displays characteristic bands at ~618 cm^{-1} and 1610 cm^{-1}, while the 2D-hBN flakes give a strong E_{2g} vibration at ~1380 cm^{-1}, confirming the coexistence of the two phases within the hybrid system. Complementary TEM analysis, presented in Fig. 1(b)–(g), reveals a homogeneous dispersion of nearly spherical ferrite nanoparticles embedded within the 2D-hBN matrix. Low-magnification images [Fig. 1(c)] show well-separated ferrite particles, whereas higher-magnification micrographs clearly display the contrast between the darker ferrite regions and the lighter background of hBN sheets. The corresponding fast Fourier transform (FFT) pattern [Fig. 1(d)] exhibits concentric diffraction rings consistent with the spinel lattice of the ferrite particles as well as distinct spots indicative of the hexagonal symmetry of hBN. Interfacial regions where the ferrite particles intimately contact the hBN nanosheets are highlighted in Fig. 1(e) and (f), where lattice fringes of both phases can be observed. The inset FFT of Fig. 1(f) confirms the cubic spinel ordering of the ferrite particles together with the hexagonal periodicity of hBN sheets. To further resolve these overlapping domains, inverse FFT filtering [Fig. 1(g)] was employed, to separate the hexagonal lattice structure of hBN (white/green atomic schematic) from the cubic ferrite framework (blue schematic). These combined Raman and TEM results, compared alongside the XRD peak shift discussed above, provide a compelling evidence of strong interfacial coupling and strain transfer between the ferrite spinel phase and the 2D-hBN nanosheets, which causes the observed lattice expansion and the change in magnetic response of the composite (2D-hBN/ferrofluid). We have calculated the strain transfer using TEM as well Raman Spectroscopy, as mentioned in Section S1 (SI).

Magnetic properties

The magnetic properties of the base ferrofluid and the effect of 2D-hBN incorporation were evaluated to assess their relevance to cooling performance. As shown in Fig. 2a, exfoliated 2D-hBN exhibits weak paramagnetic behavior, whereas bulk hBN is diamagnetic in nature.[38] This response originates from structural defects and edge terminations generated during exfoliation process, which creates localized spin states in the wide-bandgap lattice.[39,40] The temperature-dependent magnetization (M–T) curves (Fig. 2b) reveal the expected decrease in magnetization with increasing temperature for both fluids, characteristic of superparamagnetic ferrite nanoparticles. The 2D-hBN/ferrofluid, however, maintains a higher magnetization over the entire 150–600 K range, with a slower decay rate, indicating improved magnetic stability.

The M–H behavior of the investigated samples was examined to assess their magnetic response at room temperature. As presented in Fig. 2(c), the 2D-hBN/ferrofluid exhibits a modest increase in magnetization compared with the pristine ferrofluid. This enhancement arises from the interfacial interactions between the ferrite nanoparticles and the hBN nanosheets. The atomically smooth and chemically inert 2D hBN surface can partially passivate surface spins and reduce spin canting at the ferrite interface, resulting in a more collinear alignment of

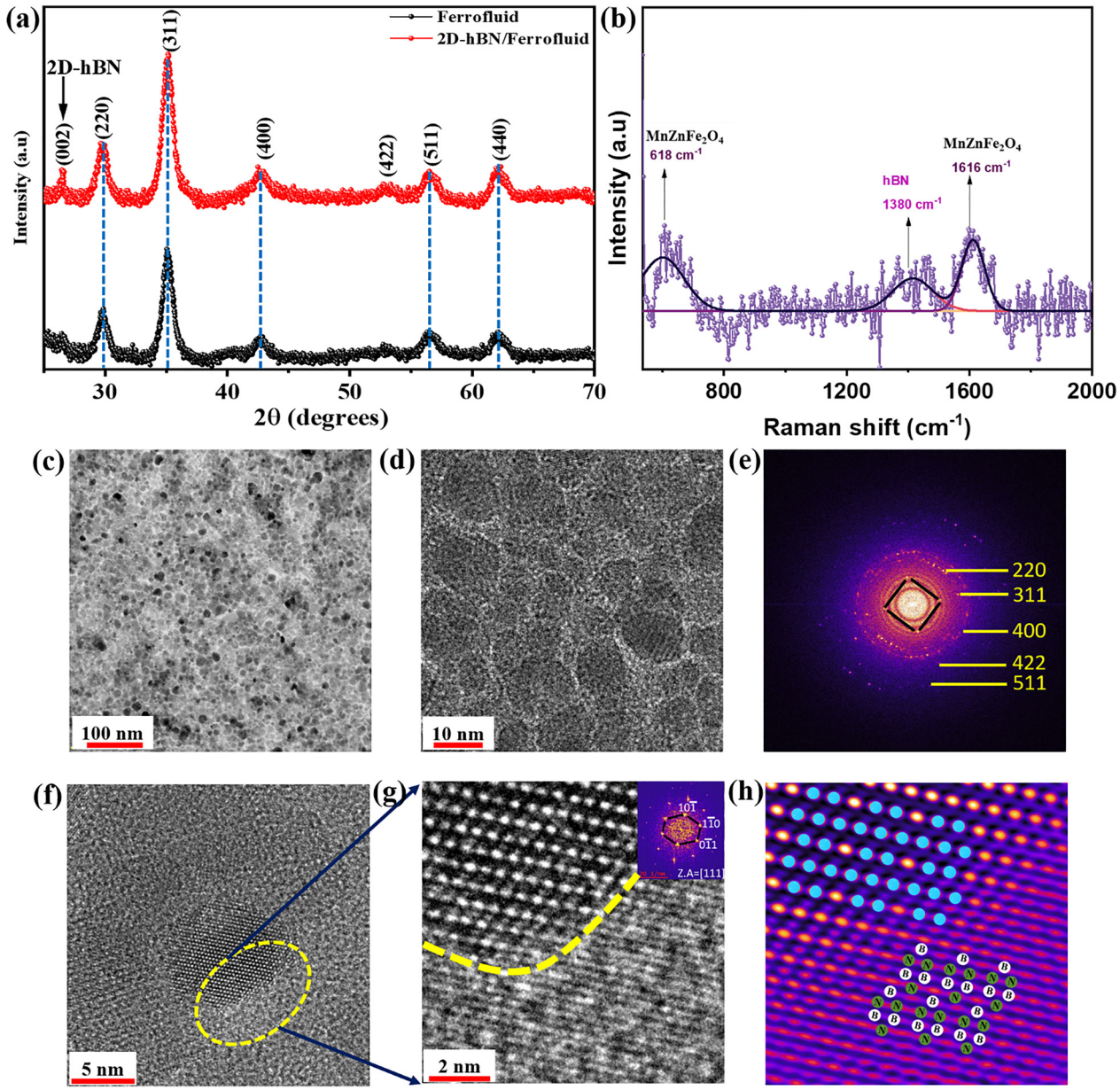

Fig. 1 (a) XRD pattern of base ferrofluid and 2D-hBN/ferrofluid showing spinel phase and hBN. (b) Raman spectra of 2D-hBN/ferrofluid sample. (c) HR-TEM image of 2D-hBN/ferrofluid sample. (d) and (e) HR-TEM image of 2D-hBN/ferrofluid sample at higher magnification and corresponding FFT (fast Fourier transform). (f) and (g) HR-TEM image of 2D-hBN/ferrofluid sample showing the interface between hBN flake and ferrite particle (FFT pattern-inset). (h) Inverse FFT of HR-TEM image (shown in (g).

magnetic moments. In addition, the slight lattice expansion observed in XRD and the reduced magnetic anisotropy predicted by DFT suggest a minor redistribution of cations or strain relaxation at the interface, which may further contribute to the higher net magnetization in the 2D-hBN/ferrofluid. Recent theoretical and experimental works were able to discover and explain this effect for similar systems.[41,42] These interfacial interactions collectively sustain stronger magnetic coupling and stable magnetization, rendering the 2D-hBN/ferrofluid system promising for magnetothermal applications where magnetic stability under cyclic operation is critical.[43–45]

In addition to magnetic measurements, the thermal conductivity of both ferrofluids was evaluated, as efficient heat transport is critical for achieving effective cooling. Higher thermal conductivity directly facilitates faster heat dissipation and thereby enhances the overall cooling performance of the device. The incorporation of 2D-hBN was specifically targeted to exploit its exceptionally high intrinsic thermal conductivity (reported up to $\sim$300 W m^{-1} K^{-1}).[21] As shown in Fig. 2(d), this strategy proved effective: the thermal conductivity of the ferrofluid is $\sim$0.294 $\pm$ 0.005 W m^{-1} K^{-1}, whereas the 2D-hBN/ferrofluid reaches $\sim$0.582 $\pm$ 0.015 W m^{-1} K^{-1}, representing

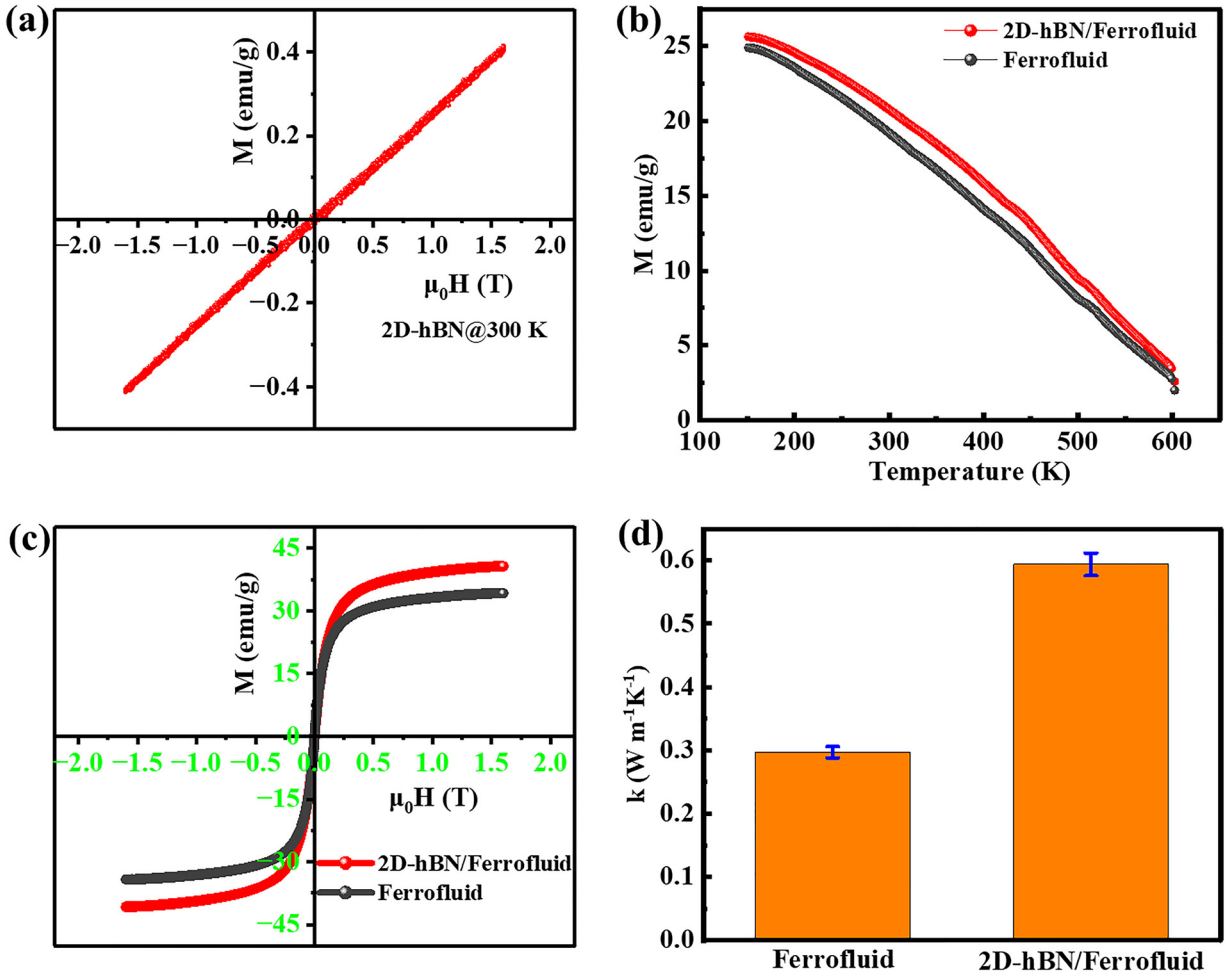

Fig. 2 (a) *M*–*H* (magnetic hysteresis) of 2D-hBN at 300 K. (b) *M*–*T* (magnetization *vs.* temperature) behavior of ferrofluid and 2D-hBN/ferrofluid at 1000 Oe. (c) *M*–*H* behavior of ferrofluid and 2D-hBN/ferrofluid. (d) The thermal conductivity of ferrofluid and 2D-hBN/ferrofluid.

nearly a twofold enhancement. This substantial improvement underscores the dual role of 2D-hBN in simultaneously boosting both the magnetic response and the heat-transfer capability of the ferrofluid, which is essential for magnetothermal cooling applications. Because the introduction of 2D-hBN simultaneously leads to a measurable increase in the magnetic response, density functional theory (DFT) calculations were carried out to gain atomic-scale insight into the origin of this effect. DFT calculations allow us to identify how defect states, interfacial charge transfer, and spin polarization within hBN or at the hBN-ferrite particles interface contribute to the observed increase in magnetization. DFT calculations clarified that doping with boron nitride diminishes the magneto crystalline anisotropy energy (MAE) of the spinel component. Consequently, a reduced particle aggregation in the liquid is anticipated due to a diminished MAE. This results in enhanced thermal agitation of particles (random spin orientation at elevated temperatures) and improved heat transmission from the area where particle magnetizations are aligned by the external magnetic field due to higher magnetic anisotropy impact. This picture correlates with prior research indicating that the optimal conditions for efficient magnetic cooling include high saturation magnetization, low magneto-crystalline anisotropy of magnetic nanoparticles, and reduced viscosity of the ferrofluid.[46] The first aspect remains uninfluenced, but the other two become captivated by BN doping. The combination of the experimental measurements and first-principles modelling therefore clarifies that, 2D-hBN not only improves heat transport but also alters the local electronic environment in a way that enhances the overall magnetic properties of the ferrofluid.

Theoretical results

To simulate the magnetic properties of the ferrofluid, the cells of the $MnZnFe_2O_4$ and BN crystals were used, the initial structures of which were taken from the electronic resource (https://materialsproject.org). $MnZnFe_2O_4$ crystallizes into the structure of the spinel mineral with a cubic unit cell of 8.5621 Å, and belongs to the space group (*Fd3m*). The spinel structure is one of the dense cubic packings in the ball model (Fig. S8(a)). The $MnZnFe_2O_4$ unit cell contains four Mn^{+2} and Zn^{+2} divalent ions located in the first type of interstitial sites (see Fig. S8(b)) and sixteen Fe^{+3} trivalent ions located in the second type of interstitial sites (see Fig. S8(c)). The spinel crystal in the magnetic phase is a ferrimagnet: the

magnetic moments of the ions in the centers of the tetrahedra and octahedra are antiparallel.

Boron nitride has a graphene-like structure with hexagonal cell parameters: $a = b = 2.51243$ Å, $c = 7.70726$ Å. The distance between the van der Waals layers is about 3.85 Å (see Fig. 3(a)). To simulate the interaction between spinel and boron nitride, a 2×2 supercell was created, consisting of incomplete spinel cells and a surface layer of boron nitride. The resulting structure is shown in Fig. 3(b). The relaxation of the parameters of the equilibrium structures and subsequent theoretical studies were carried out within the framework of the density functional theory (DFT)[47] method using the VASP software package. The method of calculating the electronic structure is based on the Rayleigh-Ritz variational principle. First-principles calculations were performed using the generalized gradient approximation (GGA) with ultra-soft PBE potentials. This approximation corrects many inaccuracies of the local density approximation (LDA). The VASP software package used applies the projected augmented wave (PAW) method, and the expansion of wave functions in the basis of the attached plane waves. The PAW method successfully combines the accuracy of full-electron methods with the efficiency of full-potential methods. All the visualizations in this work were performed in the VESTA software package.[48] The main goal of the theoretical study was to explain the phenomenon of increasing the magnetization of a ferrofluid when boron nitride is added to it. We hypothesized that the interaction between boron nitride particles and spinel ferrite particles causes changes in the magnetic anisotropy of the latter in several atomic layers adjacent to the boron nitride. To test this assumption within the framework of non-collinear magnetism, we calculated the energies of the $MnZnFe_2O_4$ spinel supercell with boron nitride at two positions of the magnetic moments: in the plane of the $\vec{a}$, $\vec{b}$ vectors (see Fig. 3(c)) and in the perpendicular direction, along the vector $\vec{c}$ (see Fig. 3(d)). Similar calculations were performed for the supercell without hBN. The results are shown in Table 2.

As can be seen from Table 2, the axis of the easiest magnetization of the samples coincides with the direction of

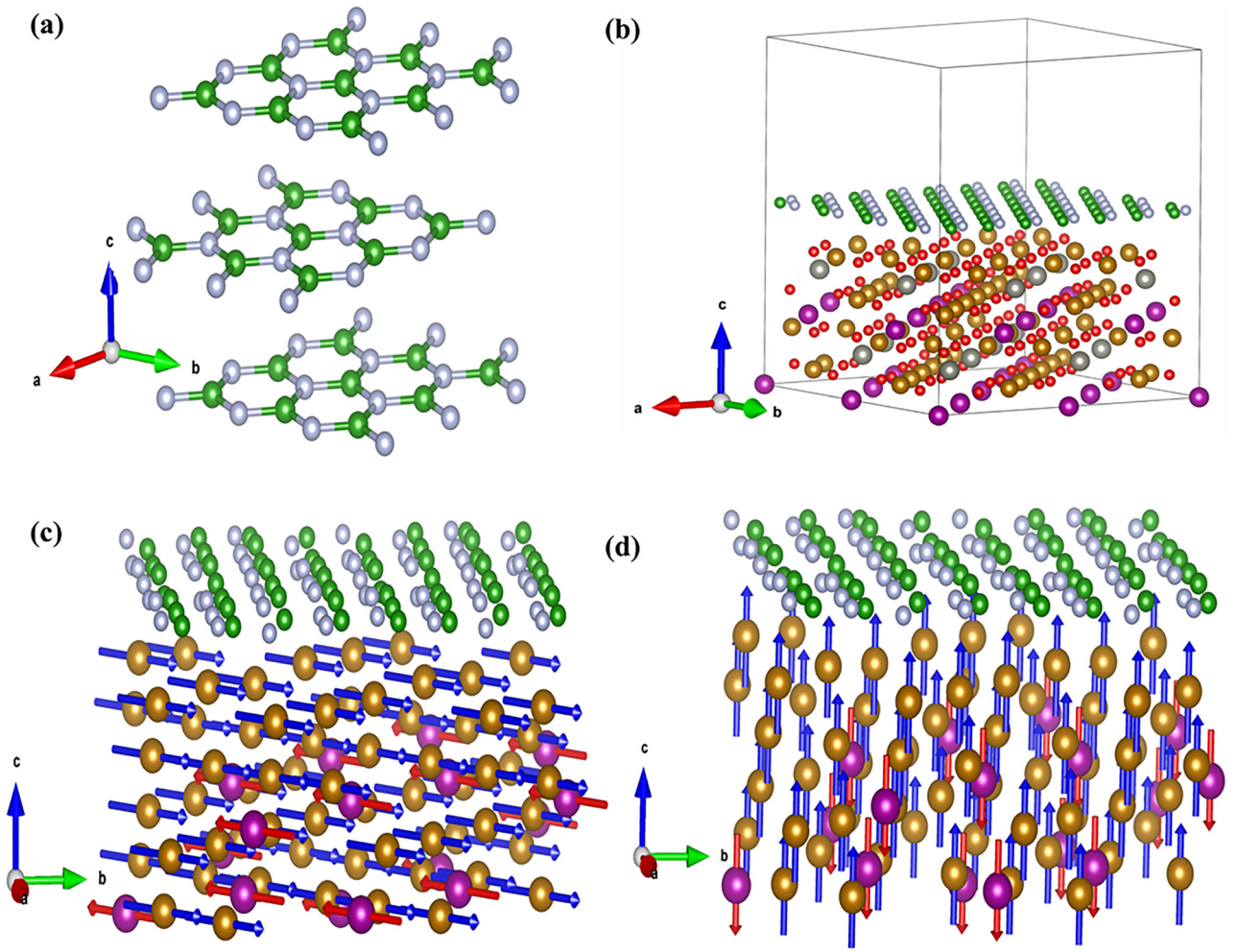

Fig. 3 (a) van der Waals layers of boron nitride. B ions are shown in green, and N ions are shown in blue. (b) A supercell consisting of four incomplete spinel cells and a layer of boron nitride. (c) Magnetic sublattice of Mn and Fe ions with magnetic moments lying in the plane of vectors $\vec{a}$, $\vec{b}$ (d) magnetic sublattice of Mn and Fe ions with magnetic moments lying along the direction of the vector $\vec{c}$.

Table 2 Results of calculations of the magnetic anisotropy of the Mn–Zn–ferrite spinel layer and the Mn–Zn–ferrite and hBN layers

Material	Supercell energy, eV. The magnetic moments of the ions lie in the plane of the $\vec{a}$, $\vec{b}$ vectors.	Supercell energy, eV. The magnetic moments of the ions lie along the $\vec{c}$ vector.	Magnetic anisotropy energy difference ΔE, eV.
$MnZnFe_2O_4$	−1473.14	−1480.52	7.38
$MnZnFe_2O_4$ + hBN	−2389.10	−2392.04	2.94

the $\vec{c}$ vector, and the axis of the hardest magnetization lies in the plane of the $\vec{a}$, $\vec{b}$ vectors. The presence of boron nitride on the $MnZnFe_2O_4$ ferrite spinel reduces the magnetic anisotropy in the surface layer by a factor of 2.5, making $MnZnFe_2O_4$ a more magnetically soft material and generally increasing the magnetization of the ferrofluid in an external magnetic field.

The incorporation of 2D-hBN into the ferrofluid reduces the magneto-crystalline anisotropy energy (MAE) of the spinel nanoparticles. As a consequence, the particles are less prone to magnetic-field-induced aggregation in the liquid, supporting more stable dispersion. The reduced MAE also enhances thermal agitation of the particle moments at elevated temperatures, facilitating more effective heat transfer from regions where the magnetization aligns with the applied field. This interpretation is consistent with earlier studies showing that efficient magnetic cooling requires high saturation magnetization, low magneto-crystalline anisotropy, and low ferrofluid viscosity.[46] In our system, the saturation magnetization is largely preserved, while both the anisotropy and the effective viscosity-associated behavior are influenced by the presence of 2D-hBN.

Device performance

Effect of magnetic field on cooling

For proof-of-concept testing, a prototype device was fabricated to evaluate the performance of magnetic cooling. The schematic of the experimental setup is presented in Fig. 4(a) (also see Fig. S2). The device consists of a copper-based circular loop designed to contain the ferrofluid. One segment of the loop includes a filling port with a sealed cap, enabling the introduction and secure containment of the ferrofluid and serving as a heat sink (at ambient temperature), which is positioned to facilitate efficient heat dissipation. Directly opposite this filling port, a Kanthal resistive wire (heat load) connected to a source meter serves as the controlled heat source, allowing precise application of thermal load. A permanent magnet is strategically placed near the heat load to induce thermomagnetic convection, which is required for fluid circulation. To monitor the thermal response of the system, five calibrated thermocouples (TC) are attached at critical locations: two near the heat source to accurately predict the heat source temperature (TC-1 and TC-2). The reason behind taking two thermocouples at heat source is to get more accurate value of temperature at heat source location, by doing average. Further, two thermocouples along the section between the heat source and the heat sink (TC-3 and TC-4), and one positioned near the heat sink itself (TC-5) (Fig. 4(a) and Fig. S2). This configuration enables accurate measurement of the temperature gradient and overall cooling efficiency.

As illustrated in Fig. 4(a), the magnetic response of the ferrofluid varies along with the temperature gradient. Near the heat sink, where the fluid is colder, the magnetization is highest, whereas near the heat load, the elevated temperature results in a significantly reduced magnetization. Under the applied magnetic field, this spatial variation in magnetization produces a magnetic body force. This force drives the colder, more strongly magnetized fluid toward the magnet and displaces the warmer, weakly magnetized fluid toward the heat sink. After releasing the heat at the sink, the fluid cools and regains higher magnetization, completing a thermomagnetic convection loop that enables continuous heat transport.

To evaluate the device performance under different thermal loads, experiments were conducted at three different power inputs 4.80 W, 6.95 W, and 9.45 W, using both the base ferrofluid and the 2D-hBN/ferrofluid (Fig. 4(b)–(g)). In the first set of measurements, the system temperature was recorded under ambient conditions for 5 minutes, followed by 20 minutes of heating at the selected power levels, after which the power supply was turned off to allow the device to return to ambient temperature. In the second condition, the procedure was repeated with a permanent magnet carefully positioned adjacent to the heat load (Fig. 4a) to introduce a magnetic field. The key distinction between these two conditions is therefore the presence or absence of the magnetic field. As shown in Fig. 4(b) for the 2D-hBN/ferrofluid, the red curve represents the measurement without an applied field ($\mu_o H$ = 0 T), while the blue curve corresponds to the case with a magnetic field ($\mu_o H$ = 0.30 T). A clear temperature difference of ∼22 °C was observed between the two conditions, indicating the enhanced heat removal achieved through magnetically induced thermomagnetic convection. This temperature difference directly reflects the cooling capability of the device, demonstrating that the applied magnetic field strengthens the magnetic body force and accelerates heat transport away from the heat source. A clear dependence of cooling performance on the applied heat load was observed. For the 2D-hBN/ferrofluid, the temperature drop increased to ∼28 °C at 6.95 W and further to ∼35 °C at 9.45 W as shown in Fig. 4(c) and (d), respectively. This trend arises because a stronger thermal gradient enhances the difference in magnetic susceptibility across the loop, thereby intensifying the thermomagnetic convective flow. Comparatively, base ferrofluid demonstrated reduced cooling efficiency, achieving temperature drops of ∼13 °C at 4.80 W, ∼20 °C at 6.95 W, and ∼23 °C at 9.45 W as shown in Fig. 4(e), (f), and (g), respectively. The superior performance is attributed to its higher thermal conductivity, which facilitates faster heat transport once the magnetically induced body force initiates circulation.

These results underscore the synergistic effect of increased thermal load and magnetic field strength in amplifying magneto-thermal convection and highlight the advantage of 2D-hBN reinforcement in achieving enhanced cooling efficiency across a wide range of operating conditions. To provide a direct comparison, the

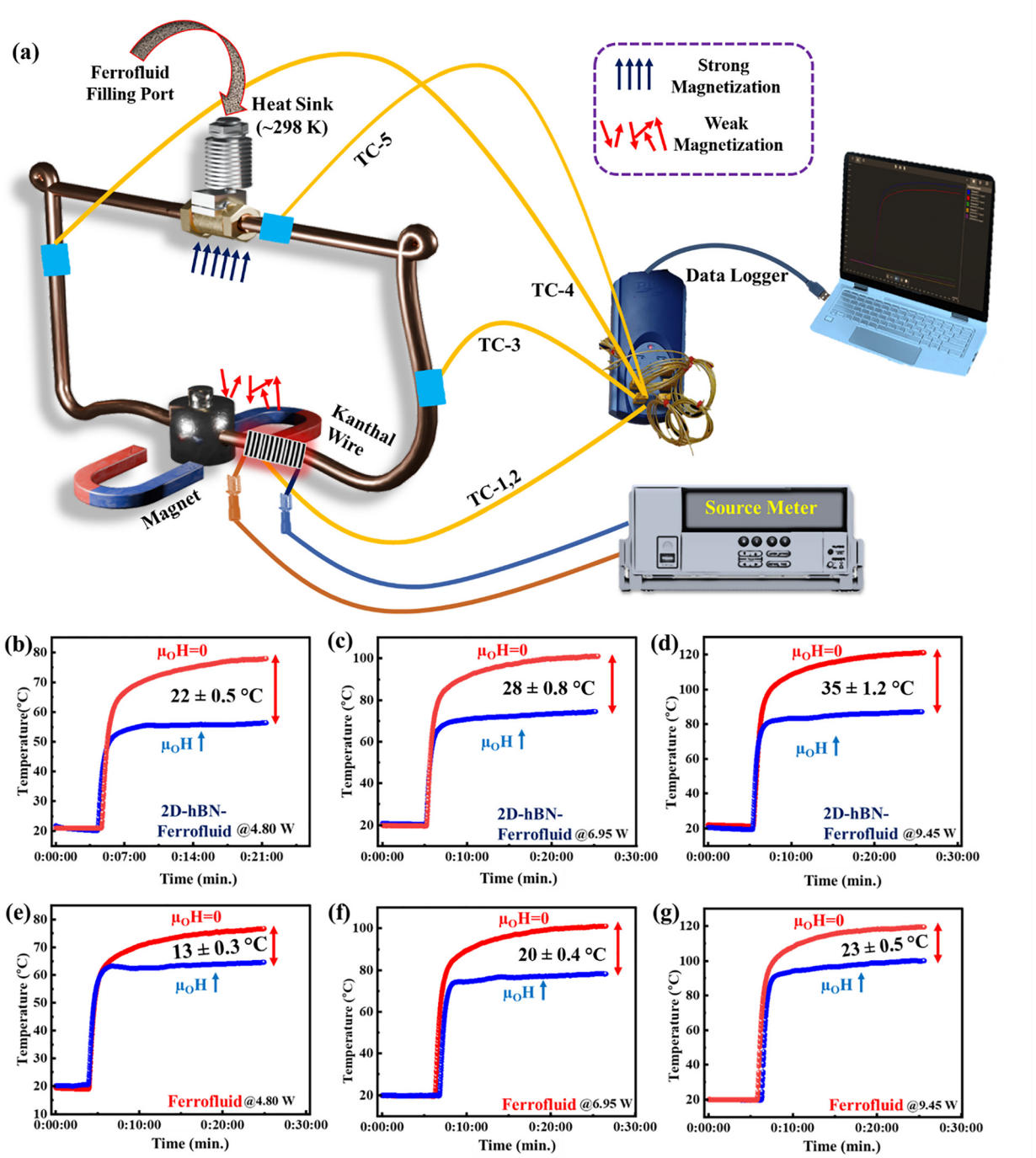

Fig. 4 (a) Schematic of the experimental device comprising a Cu-based circular loop, a permanent magnet, and a Kanthal wire connected to a source meter to provide a controlled heat load. Five thermocouples are mounted on the Cu loop and linked to a data logger, which is interfaced with a computer for real-time temperature monitoring. (b)–(d) The effect of application and removal of the magnetic field (2 times) on the cooling performance of the device for 2D hBN/ferrofluid at various power loads (4.80 to 9.45 W). (e)–(g) The effect of application and removal of the magnetic field (2 times) on the cooling performance of the device for base ferrofluid at various power loads (4.80 to 9.45 W).

cooling performance of the base ferrofluid and the 2D-hBN/ferrofluid is summarized in Fig. 5, which illustrates the variation in temperature drop with the applied heat load. At all power levels, the 2D-hBN/ferrofluid consistently exhibits higher cooling efficiency than the base fluid. A comparison with previously reported ferrofluid-based cooling studies and the related discussion is provided in Section S2 of the SI (Fig. S9). Along with this we have provided a detailed comparison of properties such as thermal conductivity, particle size, and volume percent of nanoparticle of various ferrofluids, as shown in Table 3.

Overall, the 2D-hBN/ferrofluid delivers higher cooling capability across all tested heat loads, demonstrating the beneficial

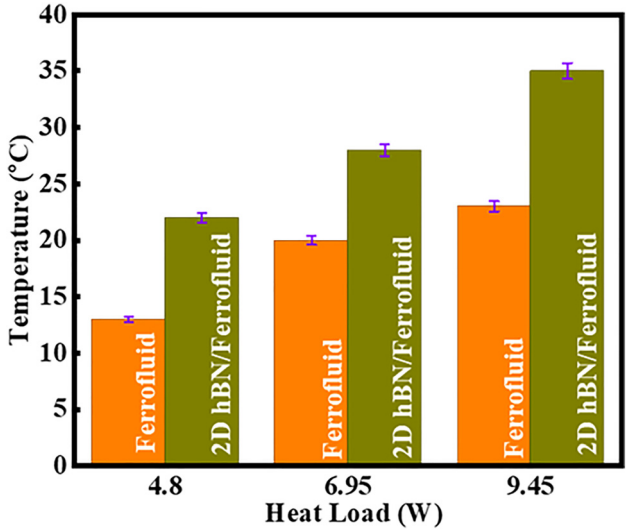

Fig. 5 Maximum cooling achieved by the base ferrofluid and the 2D-hBN/ferrofluid at heat loads of 4.80, 6.95, and 9.45 W under a 0.30 T magnetic field. The 2D-hBN/ferrofluid consistently shows a larger temperature drop than the base ferrofluid at all heat loads. Error bars represent measurement uncertainty.

role of hBN incorporation. The improvement arises from the enhanced thermal conductivity provided by the 2D-hBN, which enables more efficient heat extraction from the heated section and faster transport of that heat toward the cooled region. Additionally, the increased magnetization and reduced anisotropy of the 2D-hBN/ferrofluid support stronger thermomagnetic driving forces, further contributing to its superior cooling performance. The strong interfacial coupling between hBN nanosheets and ferrite nanoparticles reinforces efficient heat transfer within the hybrid ferrofluid. To confirm the circulation of the ferrofluid upon magnetic field application, temperature measurements were recorded using thermocouples TC-3 and TC-4, as shown in Fig. 4(a). As illustrated in Fig. S10, once the magnetic field is applied, the ferrofluid begins to circulate – resulting in an initial temperature rise at TC-3 (blue), which subsequently decreases as the 2D-hBN/ferrofluid approaches the heat sink region (green). Furthermore, as the 2D-hBN/ferrofluid reaches TC-3, TC-4 (violet), and TC-5 (heat sink) a further temperature drop is observed, confirming efficient heat transfer and circulation within the system.

Cooling performance under repeated magnetic field switching

A comparative investigation was conducted between the base ferrofluid and the 2D-hBN/ferrofluid to evaluate their cooling performance. Because the ferrofluid is water-based, the heat load was first stabilized at a safe operating range of 110–120 °C. After the system reached equilibrium, an external magnetic field ($\mu_o H$) was applied as illustrated in Fig. 6(a). Upon field activation, a rapid temperature drops to nearly 34 °C was observed within 2–3 minutes, followed by a steady state over the next 5 minutes. Simultaneously, the heat sink temperature (blue line) increased slightly before stabilizing, confirming the transfer of heat from the load to the sink. This dynamic cooling behaviour arises from the magnetothermal convection of the ferrofluid. The suspension contains thermomagnetic nanoparticles whose magnetization decreases with increasing temperature and becomes paramagnetic above their Curie point. When a magnetic field is applied, the cooler, more strongly magnetized fluid near the heat sink is drawn toward the magnet positioned adjacent to the heat source. As this fluid absorbs heat, its magnetic susceptibility decreases, reducing its attraction to the magnet and allowing it to be displaced by cooler incoming fluid. The heated fluid then flows toward the heat sink, where it releases the absorbed energy and cools down, thereby sustaining a continuous circulation that drives efficient heat transport. In comparison to the ferrofluid without 2D-hBN, the cooling was around 28 °C only, as shown in Fig. S11(a). The incorporation of 2D-hBN further enhances this process by improving thermal conductivity and facilitating faster heat dissipation.

To verify the repeatability of the process, the magnetic field was first removed, allowing the system temperature to rise back to approximately 110 °C within a few minutes. Reapplying the field triggered another rapid cooling cycle, and its subsequent removal again restored the initial temperature after about ten minutes. The device performance was further assessed under a reduced magnetic field strength of 0.27 T. As shown in Fig. 6(b), this lower field caused a temperature drop of about 25 °C in the 2D-hBN/ferrofluid, compared with a 22 °C drop in the base ferrofluid (Fig. S11(b)). In both cases, the heat-sink temperature showed a slight initial increase before stabilizing, confirming the system's effective and consistent heat-transfer capability. As the magnetic field strength was further decreased, the cooling capability of the 2D-hBN/ferrofluid declined more sharply than that of the base fluid. At 0.24 T, the temperature drops in the 2D-hBN sample reduced to ~16 °C (Fig. 6c), compared with

Table 3 Comparative study of thermal conductivity, particle size, volume percent of various ferrofluid

Material	Particle size (nm)	Volume %	Thermal conductivity (W m^{-1} K^{-1})	Ref.
Fe_3O_4@core shell nanoparticles	~7–28	0.7	1.54	30
Fe_3O_4	~5–25	0.7	1.80	30
Fe_3O_4	5	0.6	0.18	49
$CoFe_2O_4$	25	5	0.88	50
$CoFe_2O_4$	25	1	0.59	50
Fe_2O_3	1.5	12.6	0.21	51
Fe_2O_3@sunflower oil	1.5	12.6	0.18	51
Mn–Zn–ferrite	3–5	1–4	0.294 ± 0.005	Present work
2D-hBN/ferrofluid	~3–5	1–4, 1 wt% 2D-hBN	0.582 ± 0.015	Present work

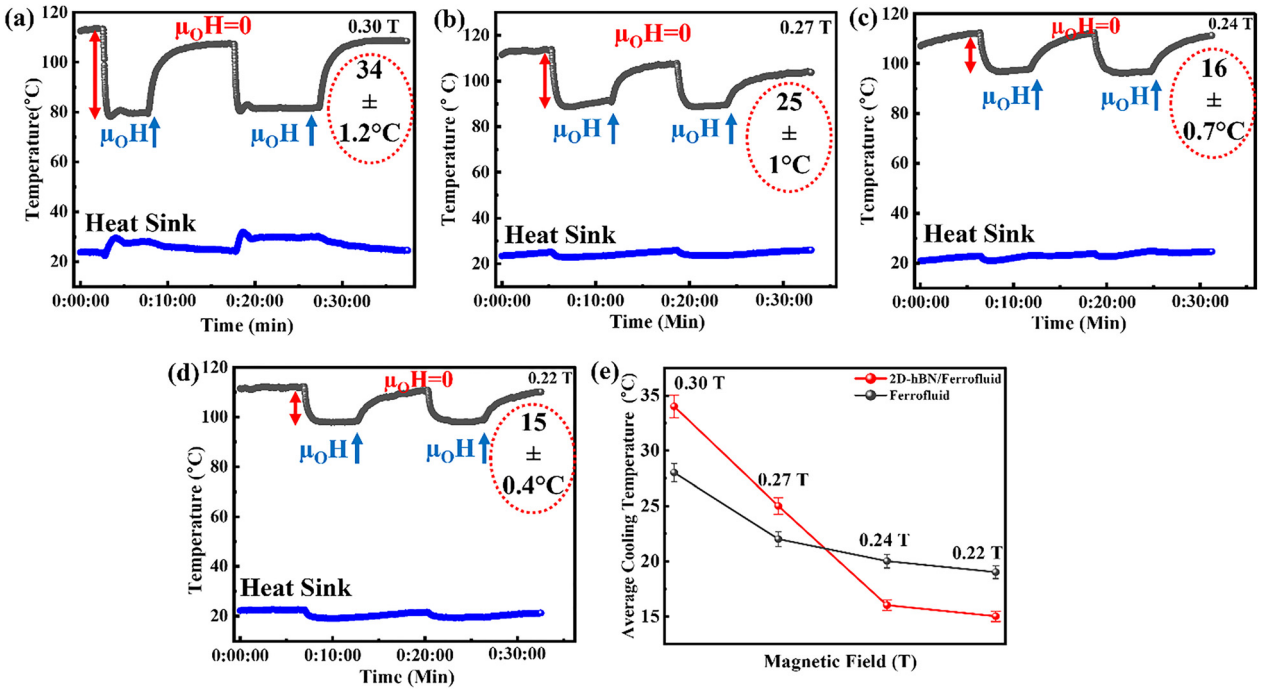

Fig. 6 (a)–(d) The effect of application and removal of the magnetic field (2 times) on the cooling performance of the device at various magnetic fields (0.30 to 0.22 Tesla). The grey curves correspond to the temperature near the heat load, and the blue curves correspond to the heat-sink temperature. The temperature drops decrease with decreasing magnetic field strength. (e) Summary of the cycling cooling achieved by the 2D-hBN/ferrofluid (red) and the base ferrofluid (black) as a function of magnetic-field strength.

~20 °C for the base ferrofluid (Fig. S11(c)). A similar trend was observed at 0.22 T, where the cooling decreased to ~15 °C in the 2D-hBN/ferrofluid (Fig. 6(d)) and ~18.5 °C in the base ferrofluid (Fig. S11(d)). At lower magnetic fields, the magnetically induced body force becomes too weak to effectively circulate the more viscous 2D-hBN/ferrofluid, as shown in Fig. S3. Although the hybrid fluid has higher thermal conductivity, its increased viscosity requires a stronger magnetic force to sustain flow. At high fields (0.30 T), this force is sufficient, and the thermal advantage dominates; however, at 0.22–0.24 T, the reduced force cannot overcome viscous resistance, leading to lower cooling performance than the base ferrofluid (Fig. 6(e)). In the hybrid system, the incorporation of two-dimensional hBN nanosheets further enhances heat transport due to their intrinsically high in-plane thermal conductivity and large surface area. The dispersed nanosheets act as additional thermal bridges within the fluid, enabling more efficient heat dissipation from the heated region. Consequently, under sufficiently strong magnetic fields, the combined effect of magnetically induced nanoparticle structuring and enhanced thermal conduction through the hBN nanosheets results in improved cooling performance. This synergistic interaction between magnetic field-driven particle dynamics and nanosheet-assisted heat transport provides an important physical basis for the observed enhancement in magnetothermal cooling behaviour.

The combined action of thermomagnetic convection and high interfacial thermal conductivity of 2D-hBN/ferrofluids enables efficient, pump-free heat transfer under moderate fields and heat loads. These findings position 2D-hBN/ferrofluids as a promising class of functional cooling media with scalability across multiple regimes – from localized electronic modules to large-area thermal management systems, including data-centre cooling architectures. The current study employs a simple device to demonstrate the effect on cooling performance. However, more complex, or advanced system designs, such as those reported in the literature,[15,16] could potentially lead to further enhancement in cooling performance and should be explored in future work.

Conclusions

We have developed and systematically evaluated a 2D-hBN/ferrofluid that exhibits simultaneous improvements in thermal conductivity and magnetic response, enabling significantly stronger magnetothermal cooling. TEM analysis confirms the uniform dispersion of exfoliated hBN nanosheets and their intimate contact with the ferrite nanoparticles, while Raman spectroscopy verifies the structural integrity of the 2D-hBN after incorporation. Magnetic measurements reveal a slight increase in magnetization, and DFT calculations show a reduction in interfacial magnetic anisotropy, consistent with the observed enhancement in magnetic response. The hybrid fluid shows a near-doubling of thermal conductivity (0.294 to 0.582 W m^{-1} K^{-1}) relative to the pristine ferrofluid. In prototype device tests, the 2D-hBN/ferrofluid delivered a maximum temperature drop of ~34 °C under a 0.30 Tesla magnetic field and provided ~40–70% higher cooling across the examined heat loads. The consistent response under

cyclic magnetic-field operation highlights the reliability of the hybrid fluid.

The present work provides experimental validation of enhanced cooling performance upon the addition of 2D-hBN; however, a comprehensive analysis and direct comparison with existing cooling methods remain to be carried out in future studies. In particular, detailed energy analysis and life cycle assessment (LCA) will be necessary to evaluate the overall environmental impact and practical viability of this approach. Overall, these results establish 2D-hBN-functionalized ferrofluids as a promising class of magnetothermal working fluids for high-heat-flux cooling applications.

Author contributions

NT – conceptualization, data curation, formal analysis, investigation, writing – original draft, methodology, SG – investigation, data curation; AK and AAS – software, validation, visualization; CST – resources, writing – review & editing, supervision; VC – conceptualization, writing – review & editing, funding acquisition, project administration, resources, supervision.

Conflicts of interest

The authors declare no conflicts of interest.

Data availability

The data supporting this article have been included as part of the supplementary information (SI). Supplementary information is available. Mn-Zn-Ferrite particle size distribution, Device Image, Viscosity measurements, SEM-EDS analysis, Structural characterization of 2D-hBN, Strain Measurement, Comparative study of cooling efficiency, and Cooling performance of base ferrofluid. See DOI: https://doi.org/10.1039/d6tc00041j.

Acknowledgements

The authors acknowledge the support of the Areas of Advance Nano, Materials, and Production at Chalmers University of Technology, and the Åforsk Foundation Sweden (Ref.nr 24-571). C. S. T. acknowledges Core research grant of SERB, India, STARS projects by MHRD-India, DAE Young Scientist Research Award (DAEYSRA), and the AOARD (Asian Office of Aerospace Research and Development) grant no. FA2386-21-1-4014, and Naval research board for funding support. Calculations by Kartsev A.I. have been supported by the RUDN University Scientific Projects Grant System, project no. 011621-2-000. The Far Eastern Computing Resource Share Resource Centre (https://cc.dvo.ru; accessed March 20, 2022) was utilised to get the results provided in this paper. The ''Data Centre of FEB RAS'' (Khabarovsk) Shared Facility Centre resources were used to process the obtained data.

References

1 A. L. Moore and L. Shi, Elsevier, 2014, preprint, DOI: 10.1016/j.mattod.2014.04.003.
2 M. A. Rahman, S. M. M. Hasnain, P. Paramasivam and A. G. Ayanie, Royal Society of Chemistry, 2024, preprint, DOI: 10.1039/d4ra05845c.
3 R. Cheng, Q. Wang, Z. Wang, L. Jing, A. V. Garcia-Caraveo, Z. Li, Y. Zhong, X. Liu, X. Luo, T. Huang, H. S. Yun, H. Salihoglu, L. Russell, N. Kazem, T. Chen and S. Shen, *Nat. Commun.*, 2025, 794.
4 W. Dai, Y. Wang, M. Li, L. Chen, Q. Yan, J. Yu, N. Jiang and C. Te Lin, John Wiley and Sons Inc, 2024, preprint, DOI: 10.1002/adma.202311335.
5 M. D. Cowley, 1989, preprint, DOI: 10.1017/S0022112089220773.
6 R. Ganguly, S. Sen and I. K. Puri, *J. Magn. Magn. Mater.*, 2004, **271**, 63–73.
7 S. Afkhami, A. J. Tyler, Y. Renardy, M. Renardy, T. G. St. Pierre, R. C. Woodward and J. S. Riffle, *J. Fluid Mech.*, 2010, **663**, 358–384.
8 J. Philip, P. D. Shima and B. Raj, *Appl. Phys. Lett.*, 2007, 203108.
9 V. B. Varma, M. S. Pattanaik, S. K. Cheekati and R. V. Ramanujan, *Energy Convers. Manage.*, 2020, 113465.
10 V. Chaudhary, Z. Wang, A. Ray, I. Sridhar and R. V. Ramanujan, *J. Phys. D: Appl. Phys.*, 2016, **50**, 03LT03.
11 O. Mahian, E. Bellos, C. N. Markides, R. A. Taylor, A. Alagumalai, L. Yang, C. Qin, B. J. Lee, G. Ahmadi, M. R. Safaei and S. Wongwises, Elsevier Ltd, 2021, preprint, DOI: 10.1016/j.nanoen.2021.106069.
12 O. Mahian, A. Kianifar, C. Kleinstreuer, M. A. Al-Nimr, I. Pop, A. Z. Sahin and S. Wongwises, 2013, preprint, DOI: 10.1016/j.ijheatmasstransfer.2013.06.010.
13 T. T. Baby and S. Ramaprabhu, *Nanoscale Res. Lett.*, 2011, 289.
14 W. Yu, H. Xie and W. Chen, *J. Appl. Phys.*, 2010, 094317.
15 N. K. Manna, D. K. Mandal, K. Bhattacharjee, N. Dikshit, N. Biswas and A. J. Chamkha, *Phys. Fluids*, 2025, 103616.
16 D. K. Mandal, N. K. Manna, N. Biswas, T. Rudra, R. Kumar and A. C. Benim, *Int. J. Thermofluids*, 2026, 101515.
17 D. K. Mandal, M. K. Mondal, N. Biswas, N. K. Manna and A. J. Chamkha, *J. Magn. Magn. Mater.*, 2023, 171035.
18 A. Bhunia, D. K. Mandal, N. K. Manna, T. Rudra, S. Bhattacharyya and N. Biswas, *Eur. Phys. J.-Spec. Top.*, 2026, 7491–7521.
19 E. Bahrami, A. Dehghani Barenji, M. Esmaeilzadeh Khabazi and A. Najafi Chermahini, Elsevier B.V., 2025, preprint, DOI: 10.1016/j.rechem.2025.102655.
20 C. Wang, J. Guo, L. Dong, A. Aiyiti, X. Xu and B. Li, *Sci. Rep.*, 2016, 25334.
21 Q. Cai, D. Scullion, W. Gan, A. Falin, S. Zhang, K. Watanabe, T. Taniguchi, Y. Chen, E. J. G. Santos and L. H. Li, *High thermal conductivity of high-quality monolayer boron nitride and its thermal expansion*, 2019.
22 L. Lindsay and D. A. Broido, *Phys. Rev. B: Condens. Matter Mater. Phys.*, 2011, 155421.

23 X. Li, Y. Li, M. M. Alam, J. Miao, P. Chen, R. Xia, B. Wu and J. Qian, *J. Mater. Chem. C*, 2020, **8**, 9569–9575.
24 M. G. Rasul, A. Kiziltas, B. Arfaei and R. Shahbazian-Yassar, *Nat. Res.*, 2021, 56.
25 F. Kargar, Z. Barani, R. Salgado, B. Debnath, J. S. Lewis, E. Aytan, R. K. Lake and A. A. Balandin, *ACS Appl. Mater. Interfaces*, 2018, **10**, 37555–37565.
26 W. Jin, W. Zhang, Y. Gao, G. Liang, A. Gu and L. Yuan, *Appl. Surf. Sci.*, 2013, **270**, 561–571.
27 I. M. Joni, R. Balgis, T. Ogi, T. Iwaki and K. Okuyama, *Colloids Surf., A*, 2011, **388**, 49–58.
28 L. S. Sundar, K. V. Sharma, M. K. Singh and A. C. M. Sousa, Elsevier Ltd, 2017, preprint, DOI: 10.1016/j.rser.2016.09.108.
29 M. L. D. O. Pereira, K. C. B. Maia, W. C. Silva, A. C. Leite, A. D. D. S. Francisco, T. L. Vasconcelos, R. S. V. Nascimento and D. Grasseschi, *ACS Appl. Nano Mater.*, 2020, **3**, 5762–5772.
30 M. Imran, N. Zouli, T. Ahamad, S. M. Alshehri, M. R. Chandan, S. Hussain, A. Aziz, M. A. Dar and A. Khan, *Nanoscale Adv.*, 2021, **3**, 1962–1975.
31 M. S. Pattanaik, S. K. Cheekati, V. B. Varma and R. V. Ramanujan, *Appl. Therm. Eng.*, 2022, 117777.
32 S. Yuan, B. Toury, C. Journet and A. Brioude, *Nanoscale*, 2014, **6**, 7838–7841.
33 Z. Rafiei-Sarmazdeh, S. H. Jafari, S. J. Ahmadi and S. M. Zahedi-Dizaji, *J. Mater. Sci.*, 2016, **51**, 3162–3169.
34 T. Shen, S. Liu, W. Yan and J. Wang, *J. Mater. Sci.*, 2019, **54**, 8852–8859.
35 R. V. Gorbachev, I. Riaz, R. R. Nair, R. Jalil, L. Britnell, B. D. Belle, E. W. Hill, K. S. Novoselov, K. Watanabe, T. Taniguchi, A. K. Geim and P. Blake, *Small*, 2011, **7**, 465–468.
36 G. R. Bhimanapati, D. Kozuch and J. A. Robinson, *Nanoscale*, 2014, **6**, 11671–11675.
37 R. Chaudhary, V. Chaudhary, R. V. Ramanujan and T. W. J. Steele, *Appl. Mater. Today*, 2020, 100824.
38 D. Y. Hwang, K. H. Choi, J. E. Park and D. H. Suh, *Phys. Chem. Chem. Phys.*, 2017, **19**, 4048–4055.
39 S. Radhakrishnan, D. Das, A. Samanta, C. A. De Los Reyes, L. Deng, L. B. Alemany, T. K. Weldeghiorghis, V. N. Khabashesku, V. Kochat, Z. Jin, P. M. Sudeep, A. A. Martí, C.-W. Chu, A. Roy, C. S. Tiwary, A. K. Singh and P. M. Ajayan, *Fluorinated h-BN as a magnetic semiconductor*, 2017.
40 B. Huang and H. Lee, *Phys. Rev. B: Condens. Matter Mater. Phys.*, 2012, 245406.
41 N. Schulz, A. Chanda, G. Datt, C. S. Ong, F. Sorgenfrei, S. Ambardar, D. V. Voronine, O. Eriksson, T. Sarkar, M. V. Kamalakar, M. H. Phan and H. Srikanth, *ACS Appl. Nano Mater.*, 2023, **6**, 10402–10412.
42 M. U. Khalid, M. A. un Nabi, M. I. Arshad and N. Amin, *Ceram. Int.*, 2026, DOI: 10.1016/j.ceramint.2026.02.379.
43 M. Fan, J. Wu, J. Yuan, L. Deng, N. Zhong, L. He, J. Cui, Z. Wang, S. K. Behera, C. Zhang, J. Lai, B. M. I. Jawdat, R. Vajtai, P. Deb, Y. Huang, J. Qian, J. Yang, J. M. Tour, J. Lou, C. W. Chu, D. Sun and P. M. Ajayan, *Adv. Mater.*, 2019, 1805778.
44 P. Tang, X. Zou, S. Wang, J. Wu, H. Liu and W. Duan, *RSC Adv.*, 2012, **2**, 6192–6199.
45 G. Yang, Y. Wu, B. Zhu, J. Li, Y. Fu, D. Gao, J. Zhao and S. Ma, *Appl. Surf. Sci.*, 2019, **487**, 825–832.
46 M. S. Pattanaik, V. B. Varma, S. K. Cheekati, V. Chaudhary and R. V. Ramanujan, *Sci. Rep.*, 2021, 24167.
47 M. G. Medvedev, I. S. Bushmarinov, J. Sun, J. P. Perdew and K. A. Lyssenko, *THEORETICAL CHEMISTRY Density functional theory is straying from the path toward the exact functional*, 2017, vol. 355.
48 K. Momma and F. Izumi, *J. Appl. Crystallogr.*, 2008, **41**, 653–658.
49 M. Imran, M. M. Alam, S. Hussain, A. Abutaleb, A. Aziz, M. R. Chandan, K. Irshad, A. M. A. Al-Hagri, O. Y. Bakather and A. Khan, *Eur. Phys. J. Plus*, 2021, 136.
50 M. Ghazwani and U. Hani, *Sci. Rep.*, 2025, 6121.
51 M. Imran, A. H. Shaik, A. R. Ansari, A. Aziz, S. Hussain, A. F. Fadil Abouatiaa, A. Khan and M. R. Chandan, *RSC Adv.*, 2018, **8**, 13970–13975.